

# The survey of planetary nebulae in Andromeda (M31)

## V. Chemical enrichment of the thin and thicker discs of Andromeda: Oxygen to argon abundance ratios for planetary nebulae and HII regions

Magda Arnaboldi<sup>1</sup>, Souradeep Bhattacharya<sup>2</sup>, Ortwin Gerhard<sup>3</sup>, Chiaki Kobayashi<sup>4</sup>, Kenneth C. Freeman<sup>5</sup>, Nelson Caldwell<sup>6</sup>, Johanna Hartke<sup>7,8</sup>, Alan McConnachie<sup>9</sup>, and Puragra Guhathakurta<sup>10</sup>

<sup>1</sup> European Southern Observatory, Karl-Schwarzschild-Str. 2, 85748 Garching, Germany  
e-mail: marnabol@eso.org

<sup>2</sup> Inter University Centre for Astronomy and Astrophysics, Ganeshkhind, Post Bag 4, Pune 411007, India

<sup>3</sup> Max-Planck-Institut für extraterrestrische Physik, Giessenbachstraße, 85748 Garching, Germany

<sup>4</sup> Centre for Astrophysics Research, Department of Physics, Astronomy and Mathematics, University of Hertfordshire, Hatfield AL10 9AB, UK

<sup>5</sup> Research School of Astronomy and Astrophysics, Mount Stromlo Observatory, Cotter Road, ACT 2611 Weston Creek, Australia

<sup>6</sup> Harvard-Smithsonian Center for Astrophysics, 60 Garden Street, Cambridge, MA 02138, USA

<sup>7</sup> European Southern Observatory, Alonso de Córdova 3107, Santiago de Chile, Chile

<sup>8</sup> Sub-Department of Astrophysics, Department of Physics, University of Oxford, Denys Wilkinson Building, Keble Road, Oxford OX1 3RH, UK

<sup>9</sup> NRC Herzberg Institute of Astrophysics, 5071 West Saanich Road, Victoria, BC V9E 2E7, Canada

<sup>10</sup> UCO/Lick Observatory, Department of Astronomy & Astrophysics, University of California Santa Cruz, 1156 High Street, Santa Cruz, California 95064, USA

Received 13 June 2022 / Accepted 16 July 2022

### ABSTRACT

**Context.** The Andromeda (M31) galaxy presents evidence of recent substantial mass accretion. This is unlike what has happened in the Milky Way, which has experienced a rather quiescent evolution.

**Aims.** We use oxygen and argon abundances for planetary nebulae (PNe) with low internal extinction (progenitor ages of  $>4.5$  Gyr) and high extinction (progenitor ages  $<2.5$  Gyr), as well as those of the HII regions, to constrain the chemical enrichment and star formation efficiency in the thin and thicker discs of M31.

**Methods.** The argon element is produced in larger fractions by Type Ia supernovae compared to oxygen. We find that the mean  $\log(\text{O}/\text{Ar})$  values of PNe as a function of their argon abundances,  $12 + \log(\text{Ar}/\text{H})$ , trace the interstellar medium (ISM) conditions at the time of birth of the M31 disc PN progenitors. Thus, the chemical enrichment and star formation efficiency information encoded in the  $[\alpha/\text{Fe}]$  versus  $[\text{Fe}/\text{H}]$  distribution of stars is also imprinted in the oxygen-to-argon abundance ratio  $\log(\text{O}/\text{Ar})$  versus argon abundance for the nebular emissions of the different stellar evolution phases. We propose using the  $\log(\text{O}/\text{Ar})$  versus  $(12 + \log(\text{Ar}/\text{H}))$  distribution of PNe with different ages to constrain the star formation histories of the parent stellar populations in the thin and thicker M31 discs.

**Results.** For the inner M31 disc ( $R_{\text{GC}} < 14$  kpc), the chemical evolution model that reproduces the mean  $\log(\text{O}/\text{Ar})$  values as a function of argon abundance for the high- and low-extinction PNe requires a second infall of metal-poorer gas during a gas-rich (wet) satellite merger. This wet merger triggered the burst of star formation seen by the PHAT survey in the M31 disc,  $\sim 3$  Gyr ago. A strong starburst is ongoing in the intermediate radial range ( $14 \leq R_{\text{GC}} \leq 18$  kpc). In the outer M31 disc ( $R_{\text{GC}} > 18$  kpc), the  $\log(\text{O}/\text{Ar})$  versus argon abundance distribution of the younger high-extinction PNe indicates that they too were formed in a burst, though mostly from the metal-poorer gas. Present-day HII regions show a range of oxygen-to-argon ratios, which is indicative of spatial variations and consistent with a present-day rainfall of metal-poorer gas onto the disc with different degrees of mixing with the previously enriched ISM.

**Conclusions.** We implement the use of the  $\log(\text{O}/\text{Ar})$  versus argon abundance distribution for emission nebulae as a complement to the  $[\alpha/\text{Fe}]$  versus  $[\text{Fe}/\text{H}]$  diagram for stars, and use it to constrain the star formation efficiency in the thin and thicker discs of M31. Diagrams for M31 PNe in different age ranges reveal that a secondary infall of gas affected the chemical evolution of the M31 thin disc. In M31, the thin disc is younger and less radially extended, formed stars at a higher star formation efficiency, and had a faster chemical enrichment timescale than the more extended thicker disc. Both the thin and thicker discs in M31 reach similar high argon abundances ( $12 + \log(\text{Ar}/\text{H}) \approx 6.7$ ). The chemical and structural properties of the thin and thicker discs in M31 are thus remarkably different from those determined for the Milky Way thin and thick discs.

**Key words.** stars: AGB and post-AGB – HII regions – planetary nebulae: general – stars: abundances – galaxies: individual: M31 – galaxies: structure

## 1. Introduction

Late-type galaxies may contain kinematically distinct components, such as the ‘cold’ thin disc and the ‘hot’ thick disc found in the Milky Way (MW; e.g., Gilmore & Reid 1983) and in nearby galaxies (Yoachim & Dalcanton 2006; Comerón et al. 2019). The MW thick disc is distinct from the MW thin disc in terms of structure and chemistry, as well as age. Differences in the structural parameters (stellar masses, exponential scale lengths, and velocity dispersion) of the MW thin and thick discs are summarised in Bland-Hawthorn & Gerhard (2016). The different chemical properties are most prominent in the measured stellar  $[\alpha/\text{Fe}]$  ratios as a function of  $[\text{Fe}/\text{H}]$ , with the old MW thick disc being more metal-poor and  $\alpha$ -enriched compared to the relatively young MW thin disc (Hayden et al. 2015; Matteucci 2021). The  $\alpha$ -enriched thick disc population is found to be confined within  $R \approx 9$  kpc and is older than  $\sim 8$  Gyr (Haywood et al. 2013; Belokurov et al. 2020), whereas the outer MW disc is composed of low  $[\alpha/\text{Fe}]$  stars (Hayden et al. 2015). These properties are believed to have been set by the MW’s most recent impactful merger  $\sim 10$  Gyr ago (Belokurov et al. 2018; Helmi et al. 2018), after which the MW disc is thought to have evolved mainly by secular evolution (see e.g., Sellwood 2014).

Unlike the MW, M31 had a more turbulent history, as vividly illustrated by the many substructures identified in its inner halo by the Pan Andromeda Archeological Survey (PAndAS; McConnachie et al. 2009, 2018), including the giant stellar stream (GSS; Ibata et al. 2001). Its most recent important merger is believed to have happened  $\sim 2.5$ – $4.5$  Gyr ago (Bhattacharya et al. 2019b, hereafter Paper II). The M31 disc has a significantly steeper age-velocity dispersion (AVD) relation than the MW disc (Paper II; Dorman et al. 2015), with the velocity dispersion of the 2.5 Gyr and 4.5 Gyr old stellar populations being almost twice and three times those of the MW disc stellar populations of corresponding ages, respectively. Paper II used planetary nebulae (PNe) as kinematic tracers to identify a younger (progenitor ages  $< 2.5$  Gyr), dynamically colder disc and a distinct, older (progenitor ages  $> 4.5$  Gyr), dynamically hotter, and hence thicker, disc, with the latter having a velocity dispersion  $\sigma_{\text{M31,thick}} \approx 3 \times \sigma_{\text{MW,thick}}$  in the radial range 14–20 kpc (equivalent to the solar neighbourhood). At these radial distances ( $R_{\text{GC}} = 14$ – $20$  kpc), the population of stars 4.5 Gyr and older had velocity dispersion values  $\geq 90$  km s $^{-1}$ , which are significantly larger than even the average velocity dispersion measured for strongly turbulent discs at redshifts  $\sim 1$ – $2$ , 30, and 60 km s $^{-1}$  (see Wisnioski et al. 2015). Mergers with satellites can dynamically heat thin discs, by increasing their velocity dispersion (Quinn & Goodman 1986) and decreasing their rotational velocity, resulting in a thickened disc (Hopkins et al. 2009). Using their results, the AVD relation of the M31 disc in a radial range  $R_{\text{GC}} = 14$ – $20$  kpc was found to be consistent with the energy injected in the M31 disc by a major merger with mass ratio  $\sim 1:5$   $\sim 2.5$ – $4.5$  Gyr ago (Paper II), as predicted in the merger simulations of Hammer et al. (2018).

The different merger histories of these two spiral galaxies are seen in their large separation in the halo metallicity versus total stellar mass diagram, where the MW and M31 are placed at opposite edges of the distribution of galaxies measured by the Galaxy Halos Outer disks Substructures Thick discs and Star Structures (GHOST) survey (Monachesi et al. 2019). In simulations, the spread in halo masses and  $[\text{Fe}/\text{H}]$  values is found to be indicative of different accretion histories (D’Souza & Bell 2018)

and accreted satellite stellar mass. Independent confirmation of a recent major merger event in M31 can be sought through chemical abundances altered by merger-related processes such as gas accretion and star formation bursts (e.g., Kobayashi & Nakasato 2011).

Planetary nebulae are useful tracers for constraining the kinematics (Aniyan et al. 2018, 2021) and chemical abundances (Magrini et al. 2016; Stanghellini & Haywood 2018) over a large radial range in nearby galaxies of different morphological types (e.g., Cortesi et al. 2013; Pulsoni et al. 2018; Hartke et al. 2022). Elemental abundances of PNe shed light on the interstellar medium (ISM) conditions at the time of formation of their parent stellar population. When the PN ages are also constrained, it becomes possible to map abundance variations across different epochs of star formation in galaxies. Abundance distributions and gradients in galaxies were measured using PNe (Maciel & Koppen 1994; Magrini et al. 2016; Kwitter & Henry 2022). In the MW, negative radial oxygen abundance gradients for both the thin and thick disc were constrained using PNe (Stanghellini & Haywood 2018), indicating inside-out disc formation. With this aim, a large survey of M31 PNe was undertaken (Bhattacharya et al. 2019a, hereafter Paper I). While it is not possible to determine the  $[\alpha/\text{Fe}]$  abundance ratio in PNe for constraining the chemical evolution, different chemical enrichment timescales that result from distinct star formation histories also leave imprints in the abundance distribution of other elements (see Nomoto et al. 2013, and references therein).

Bhattacharya et al. (2022, hereafter Paper IV) measured distinct oxygen and argon abundance distributions for the thin and thicker discs in M31. They measured flat or slightly positive oxygen and argon gradients for the older, thicker disc and a negative metallicity gradient for the younger thin disc in M31. These results are consistent with a major merger with a 1:5 mass ratio for M31. In the simulations of Hammer et al. (2018), a gas-rich satellite is accreted onto M31 with an orbit along the GSS. The merger then heats the pre-existing M31 disc, generating the observed thicker disc. The cold gas accreted through the ‘wet’ merger would lead to a burst of star formation and the formation of a late, more centrally concentrated thin disc. Because of the merger-driven disc evolution, stars in the thin and thicker discs of M31 would have formed at different epochs under different chemical conditions. Those in the younger thin disc would have formed out of the pre-enriched interstellar gas in M31, mixed with metal-poorer gas brought in by the satellite.

In this paper we investigate whether the different chemical enrichments of the thicker and thin discs in M31 provide ‘smoking gun’ evidence that the secondary gas infall predicted by such a gas-rich merger took place. We use direct measurements of oxygen and argon abundances for the M31 disc PNe over the 2–30 kpc radial range to constrain the chemical enrichment and the star formation efficiency in the thin and thicker disc. We further combine the PN abundance measurements with those for the HII regions in the M31 disc already available in the literature. The oxygen and argon measurements from Paper IV are briefly presented in Sect. 2. The use of oxygen and argon abundances as chemical tracers in M31 is discussed in Sect. 3, as are the chemical enrichment timescales inferred for the two disc components. In Sect. 4 we present the constraints on the chemical evolution and formation history of M31. We address the gas content of the merging satellite in the M31 disc in Sect. 5 and conclude in Sect. 6.

## 2. Data sample, abundance measurements, and gradients

### 2.1. The PN sample in M31 with O and Ar abundances

In [Paper I](#), PN candidates were selected in a 16 sq. deg. [O III] 5007 Å narrow plus g-broad band imaging survey covering the disc and inner halo of M31, with MegaCam at the Canada-France-Hawaii telescope (CFHT). This was later expanded to cover a total of 54 sq. deg in M31 ([Bhattacharya et al. 2021](#), hereafter [Paper III](#)). Spectroscopic follow-up of a complete sub-sample of these PN candidates were carried out with the Hectospec multi-fibre positioner and spectrograph on the Multiple Mirror Telescope (MMT; [Fabricant et al. 2005](#)). Spectral range covers from 3685 Å in the blue to approximately 9200 Å in the red, with a spectral resolution in the range 850–1500.

The oxygen and argon direct abundance measurements, via the detection of the temperature sensitive line [O III] at 4363 Å, with their errors, for a magnitude limited sample of PNe in the M31 disc, are described in [Paper IV](#), which includes the catalogue with the measured quantities (their errors). We also refer to [Paper IV](#) for a comprehensive description of the PNe magnitude limited sample and the abundance gradients. In this work we extend the analysis of the oxygen and argon abundances to constrain the chemical enrichment and the star formation timescales of the discs of M31.

To this aim, we implement the identification of the thin and thicker discs in M31 of [Paper II](#) based on the ages and dynamical properties of their PN populations, and then derive their star formation histories and chemical evolution. In the M31 magnitude-limited disc PNe sample, there are 75 high-extinction, 2.5 Gyr and younger PNe associated with the more rapidly rotating thin disc, and 130 low extinction, 4.5 Gyrs and older PNe, associated with the thicker disc, which has a larger asymmetric drift. The high extinction PNe are found at smaller radii ( $R_{GC} < 22$  kpc) than the low extinction PNe, which instead cover the entire extent of the disc (out to  $R_{GC} = 30$  kpc).

We note that the structural properties of thin and thick discs in nearby spiral galaxies show thin discs embedded in thicker discs, with the latter having longer scale lengths than the thin component ([Yoachim & Dalcanton 2006](#)). This is similar to what is found for the M31 PNe 2.5 Gyr and younger sample. Furthermore, the age determined for the thicker disc in M31 falls within the age range, from 4 to 10 Gyr, determined from Lick indices for the thick discs of local spirals ([Yoachim & Dalcanton 2008](#)).

### 2.2. The PN sample in M31 as tracers of the ISM chemical properties

As a first step in using the PN oxygen over the argon ratio versus argon abundance,  $12 + \log(\text{Ar}/\text{H})$ , distribution to constrain the ISM conditions, we explore the dependence of the PNe  $\log(\text{O}/\text{Ar})$  ratio on (i) their circumstellar dust properties, (ii) initial stellar masses, and (iii) ages. According to [Ventura et al. \(2017\)](#) theoretical models, the surface oxygen in the stellar atmospheres can be modified during the Asymptotic Giant Branch (AGB) stage in two ways.

First, oxygen in the stellar atmosphere can be enriched by the third dredge-up (TDU), which may occur in 2 Gyr old stars with masses between  $1.5\text{--}3 M_{\odot}$  and metallicity in the range  $[-0.5 : 0.0]$ . In the case of the M31 disc low extinction PNe, which are

4.5 Gyr and older, with low mass  $M_* < 1.25 M_{\odot}$  (see [Paper II](#)), their measured oxygen abundance are free of alterations from post-AGB (PAGB) evolution, and TDU in particular.

Alternatively, oxygen can be depleted by hot bottom burning (HBB), which occurs in  $M_* > 3.5 M_{\odot}$  progenitors during the AGB phase. In [Paper IV](#) (see their Appendix D), we found that the contribution to the M31 disc PN sample from very young ( $< 300$  Myr old) massive ( $M > 3.5 M_{\odot}$ ) stars is negligible; therefore, there is no evidence for oxygen depletion in the current M31 disc high extinction PN sample.

In summary, the current sample of low extinction PNe in the M31 disc are too old and of low masses for TDU to occur, while there is no evidence for the presence of very young (300 Myr) massive ( $> 3.5 M_{\odot}$ ) PNe in the current high extinction PNe sample in M31, which may be affected by oxygen depletion. We refer to [Appendix A](#) for more in-depth discussion of oxygen and argon abundances in PNe.

Unlike oxygen, argon is known to be invariant during the AGB evolution ([Delgado-Inglada et al. 2014](#); [García-Hernández et al. 2016](#); [Ventura et al. 2017](#)). Given the absence of oxygen modifications due to PAGB effects in the current M31 disc PNe sample, in what follow we then proceed to use the PN oxygen and argon abundances to study the chemical properties of the ISM at the time the PN stellar progeny were formed.

### 2.3. Oxygen and argon radial gradients for thin and thicker discs in M31

In [Paper IV](#) we measured two distinct abundance distributions for the oxygen and argon, for the thin and thicker disc in M31. The mean value of the oxygen abundance for the thin disc,  $\langle 12 + (\text{O}/\text{H}) \rangle_{\text{high-ext}} = 8.57 \pm 0.03$ , is higher than that of the thicker disc,  $\langle 12 + (\text{O}/\text{H}) \rangle_{\text{low-ext}} = 8.48 \pm 0.02$ , although both distributions have large standard deviation values. Same trend for the mean values of the argon abundance: the argon abundance of the thin disc,  $\langle 12 + (\text{Ar}/\text{H}) \rangle_{\text{high-ext}} = 6.32 \pm 0.03$ , is higher than that of the thicker disc,  $\langle 12 + (\text{Ar}/\text{H}) \rangle_{\text{low-ext}} = 6.25 \pm 0.02$ . When the two abundance distributions are compared in pairs, the two-sample Anderson-Darling test rejects the null hypothesis that the two distributions of each element are drawn from the same, underlying, distribution. Hence, the two discs in M31 are chemically distinct in oxygen abundance distribution and argon abundance distribution.

Regarding the abundance gradient with radius, in [Paper IV](#) we find a steeper negative radial gradient for the oxygen abundance for the thin disc,  $(\Delta(\text{O}/\text{H})/\Delta R)_{\text{high-ext}} = -0.013 \pm 0.006 \text{ dex kpc}^{-1}$ , which is consistent with that measured for the HII regions ([Zurita & Bresolin 2012](#)). [Paper IV](#) also measured a near-flat and slightly positive radial gradient for the oxygen abundance of the thicker disc,  $(\Delta(\text{O}/\text{H})/\Delta R)_{\text{low-ext}} = 0.06 \pm 0.003 \text{ dex kpc}^{-1}$ . The measured radial gradients for the argon abundance are  $(\Delta(\text{Ar}/\text{H})/\Delta R)_{\text{high-ext}} = -0.018 \pm 0.006 \text{ dex kpc}^{-1}$  and  $(\Delta(\text{Ar}/\text{H})/\Delta R)_{\text{low-ext}} = -0.05 \pm 0.003 \text{ dex kpc}^{-1}$ , respectively. The results of [Paper IV](#) are consistent with results of previous studies ([Sanders et al. 2012](#); [Kwitter et al. 2012](#); [Peña & Flores-Durán 2019](#)), whose oxygen gradient measurements were dominated by the more numerous low-extinction PNe associated with the thicker disc. We refer to [Paper IV](#) for a more extensive comparison of these radial gradients with those of the MW and other spirals.

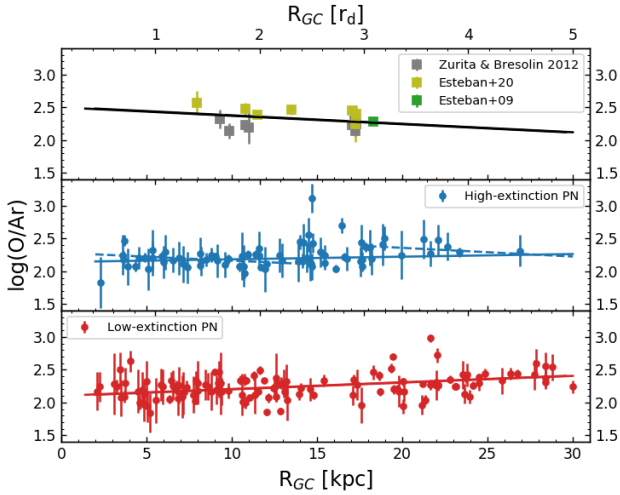


**Fig. 1.** Galactocentric radial distribution of  $\log(\text{O}/\text{Ar})$  values for HII regions (*top*) and for high- and low-extinction PNe (*middle* and *bottom*, respectively) in the M31 disc from the PN catalogue published in Paper IV. The best-fitting radial  $\log(\text{O}/\text{Ar})$  gradient is shown for HII regions (black) and high- (blue) and low-extinction (red) PNe. *Middle panel:* displays three independent linear fits for three radial ranges: the solid line is the linear fit to the entire dataset; for within 14 kpc and beyond 18 kpc, the linear fits are shown with dashed lines.

#### 2.4. Radial gradients of the $\log(\text{O}/\text{Ar})$ values

Oxygen and argon abundances are reliably measured in the M31 PNe (see Sect. 2.2, Appendix A and Paper IV). Since PNe evolve from parent stellar populations covering a range of ages, their  $\log(\text{O}/\text{Ar})$  ratios probe the ISM conditions at the different epochs of their birth, and thus provide important constraints for the chemical evolution models of the ISM (see the review by Nomoto et al. 2013 and the work by Kobayashi et al. 2020a).

In M31 we identified three population of tracers in three different age ranges. The HII regions are tracing the chemistry of the  $\sim 300$  Myr young stellar population, while the high extinction PNe, which trace the thin disc of M31, have ages 2.5 Gyrs or younger. The low-extinction PNe that are associated with the thicker disc of M31, are 4.5 Gyrs or older (see Paper II and Paper IV for further details).

Figure 1 shows the galactocentric radial distribution of the  $\log(\text{O}/\text{Ar})$  values for HII regions<sup>1</sup> (upper panel), high-extinction PNe (middle panel) and low-extinction (lower panel) PN samples, in the  $R_{\text{GC}} = 2\text{--}30$  kpc radial range. Parameters of linear fits are also noted in Table 1. We find a negative radial gradient for the HII regions, with relatively large error bars. For the low-extinction PNe, we determine a slightly positive radial gradient, with a mixture of high and low  $\log(\text{O}/\text{Ar})$  values at any radius over the 2–20 kpc radial range of the disc. For the high-extinction PNe, the figure indicates distinct  $\log(\text{O}/\text{Ar})$  distributions in three radial regions. Within  $R_{\text{GC}} < 14$  kpc,  $\langle \log(\text{O}/\text{Ar}) \rangle = 2.28 \pm 0.05$  with a slightly negative radial gradient. In the  $R_{\text{GC}} > 18$  kpc outer region  $\langle \log(\text{O}/\text{Ar}) \rangle = 2.62 \pm 0.28$  with a negative radial gradient as for the inner region. In the intermediate radial range 14–18 kpc, which includes the most

<sup>1</sup> Their oxygen and argon abundances were also determined directly using the [O III] temperature sensitive line at 4363 Å (see Esteban et al. 2009, 2020; Zurita & Bresolin 2012) within a  $R_{\text{GC}} = 17$  kpc radius. Because HII regions have high internal extinction, direct detection of the [O III] 4363 Å emission line may lead to select preferentially a relatively metal-poor population.

**Table 1.** Fitted parameters for the radial gradients of the  $\log(\text{O}/\text{Ar})$  values for HII regions (literature values) and in the M31 disc from the Paper IV M31 disc PNe sample.

Sample	$\log(\text{O}/\text{Ar})_0$	$\Delta \log(\text{O}/\text{Ar})/\Delta R$	
		dex kpc <sup>-1</sup>	dex/ $r_d$
HII regions	$2.51 \pm 0.13$	$-0.013 \pm 0.008$	$-0.078 \pm 0.049$
High-extinction PNe (all)	$2.14 \pm 0.04$	$0.004 \pm 0.003$	$0.024 \pm 0.021$
$R_{\text{GC}} \leq 14$ kpc	$2.28 \pm 0.05$	$-0.011 \pm 0.005$	$-0.072 \pm 0.032$
$R_{\text{GC}} > 18$ kpc	$2.62 \pm 0.28$	$-0.013 \pm 0.012$	$-0.08 \pm 0.075$
Low-extinction PNe	$2.1 \pm 0.05$	$0.01 \pm 0.003$	$0.063 \pm 0.016$

active star forming region in the M31 disc (Kang et al. 2009), the  $\log(\text{O}/\text{Ar})$  values have a wide spread, including the largest inferred values ( $>2.5$ ) for the PNe in our sample. We discuss the radial gradients and the constraints on the  $\log(\text{O}/\text{Ar})$  distributions of the different age ranges on the chemical evolution models for the thin and thicker disc in M31 in the following sections.

### 3. Oxygen versus argon as tracers of the enrichment history in the M31 discs

The star formation history of a galaxy leaves chemical imprints in its ISM through enrichment with different elements. The information of the ISM chemical conditions at the time of birth of a star is encoded in its element abundances. While both argon and oxygen are produced from core-collapse supernovae, argon is additionally produced by Type-Ia supernovae (Kobayashi et al. 2020a,b). Thus, even though both argon and oxygen are  $\alpha$ -elements, they do not have lockstep behaviour and the star formation histories of parent stellar populations will imprint information on the  $\log(\text{O}/\text{Ar})$  versus argon abundance,  $12 + \log(\text{Ar}/\text{H})$ , distribution of stars with different ages.

#### 3.1. M31 PN distribution in the $\log(\text{O}/\text{Ar})$ versus $12 + \log(\text{Ar}/\text{H})$ plane

The left panel of Fig. 2 shows the oxygen-to-argon abundance ratio,  $\log(\text{O}/\text{Ar})$ , versus  $12 + \log(\text{Ar}/\text{H})$  for all the M31 PNe. In order to identify the general trend in the  $\log(\text{O}/\text{Ar})$  versus argon abundance, we adopt the following procedure. We divide the high- and low- extinction PNe into bins of argon abundance,  $12 + \log(\text{Ar}/\text{H})$ , such that there are between 8 and 15 PNe in each bin. The number of PNe in each bin are chosen such that there are enough PNe in each bin to obtain a reliable dispersion in  $\log(\text{O}/\text{Ar})$  while covering the entire  $12 + \log(\text{Ar}/\text{H})$  range with as many bins as possible. The number of PNe in each bin is lower for the high-extinction PNe as they are fewer in total<sup>2</sup>. We then calculate the mean  $\log(\text{O}/\text{Ar})$  values of PNe in each  $12 + \log(\text{Ar}/\text{H})$  bin after removing the  $2 \times \sigma$  outliers from the mean<sup>3</sup>. In Tables 2 and 3 we provide the mean values of  $\log(\text{O}/\text{Ar})$  in the  $12 + \log(\text{Ar}/\text{H})$  bins, their standard deviation in bins, the error on the mean value and mean measurement error

<sup>2</sup> The bin with the largest argon abundance has fewer measurements (three) for the high-extinction PNe.

<sup>3</sup> In practice, we first calculate the mean and standard deviation from all PNe in each bin, then remove those PNe whose  $\log(\text{O}/\text{Ar})$  values are more than  $2 \times \sigma$  from the mean, and recompute the mean value for the clipped sample.

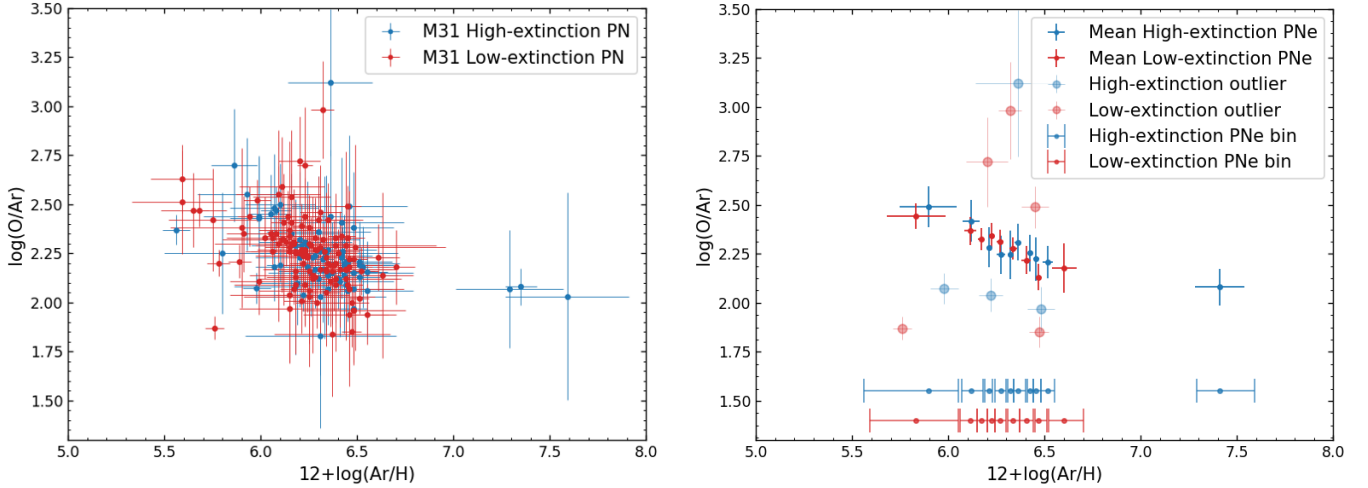


**Fig. 2.** The M31 PN distribution in the  $\log(\text{Ar}/\text{O})$  versus  $12 + \log(\text{Ar}/\text{H})$  plane. *Left:* oxygen-to-argon abundance ratio,  $\log(\text{Ar}/\text{O})$ , plotted against argon abundance for the high- (blue) and low- (red) extinction PNe in M31. *Right:* high- (blue) and low- (red) extinction PNe binned separately as a function of their  $12 + \log(\text{Ar}/\text{H})$  values. For each bin the sigma-clipped mean  $\log(\text{O}/\text{Ar})$  value added in quadrature to the mean observation error of the PNe that remain in each bin, after the sigma-clipping. Clipped PNe with  $\log(\text{O}/\text{Ar})$  values that are more than 2 sigma beyond the mean values are marked with a lighter shade. Error bars along the  $x$  axis capture the rms of PNe in each argon abundance bin. Red and blue error bars parallel to the  $x$  axis indicate the width of the bins in  $12 + \log(\text{Ar}/\text{H})$  for the low-extinction (red) and high-extinction (blue) PN samples.

**Table 2.**  $\log(\text{O}/\text{Ar})$  average values in the  $12 + \log(\text{Ar}/\text{H})$  bins, for the low-extinction PNe in M31.

$12 + \log(\text{Ar}/\text{H})$	$\log(\text{O}/\text{Ar})$	$1 \times \sigma$ $\log(\text{O}/\text{Ar})$	Error on mean $\log(\text{O}/\text{Ar})$	Mean measurement error on $\log(\text{O}/\text{Ar})$
5.83	2.44	0.10	0.02	0.07
6.11	2.37	0.10	0.03	0.08
6.17	2.33	0.09	0.02	0.06
6.22	2.34	0.12	0.03	0.07
6.27	2.31	0.10	0.02	0.07
6.34	2.28	0.12	0.03	0.06
6.40	2.22	0.09	0.02	0.08
6.47	2.13	0.16	0.04	0.07
6.60	2.18	0.10	0.03	0.12

**Notes.** Listed values include standard deviation of  $\log(\text{O}/\text{Ar})$  in each bin, error on mean  $\log(\text{O}/\text{Ar})$  values and mean measurement error in each bin.

in each bin, for the low and high-extinction PNe samples. We discuss them in turn.

In Table 2, we compare the standard deviation with the mean measurement error in each bin for the low extinction PNe: the scatter is of order  $\sqrt{2} \times$  the mean measurement error for most bins. We thus infer that there is an intrinsic scatter of the measured  $\log(\text{O}/\text{Ar})$  for the low extinction PN sample, and this scatter is of a similar order of magnitude to the mean error in the bins. We thus adopt as the error for the  $\log(\text{O}/\text{Ar})$  average value, in each bin, the error on the mean  $\log(\text{O}/\text{Ar})$  value added in quadrature to the mean observation error of the PNe, in each bin.

For the high extinction PNe in Table 3, we notice that the standard deviation is smaller than the average measured error for about half of the bins. We still adopt as the error for the  $\log(\text{O}/\text{Ar})$  average value, in each bin, the error on the mean  $\log(\text{O}/\text{Ar})$  value added in quadrature to the mean observational error in each bin, keeping in mind that the dispersion of values is smaller for  $12 + \log(\text{Ar}/\text{H})$  range 6.21–6.32, and for the larger  $[\text{Ar}/\text{H}]$  abundance values. Finally, in the right panel of

**Table 3.**  $\log(\text{O}/\text{Ar})$  average values in the  $12 + \log(\text{Ar}/\text{H})$  bins, for the high-extinction PNe in M31.

$12 + \log(\text{Ar}/\text{H})$	$\log(\text{O}/\text{Ar})$	$1 \times \sigma$ $\log(\text{O}/\text{Ar})$	Error on mean $\log(\text{O}/\text{Ar})$	Mean measurement error on $\log(\text{O}/\text{Ar})$
5.89	2.49	0.12	0.05	0.09
6.12	2.42	0.13	0.05	0.10
6.21	2.28	0.09	0.03	0.09
6.27	2.24	0.10	0.04	0.09
6.32	2.25	0.11	0.04	0.12
6.36	2.31	0.12	0.04	0.08
6.42	2.25	0.12	0.04	0.08
6.46	2.23	0.09	0.03	0.10
6.52	2.21	0.11	0.04	0.07
7.41	2.08	0.02	0.01	0.09

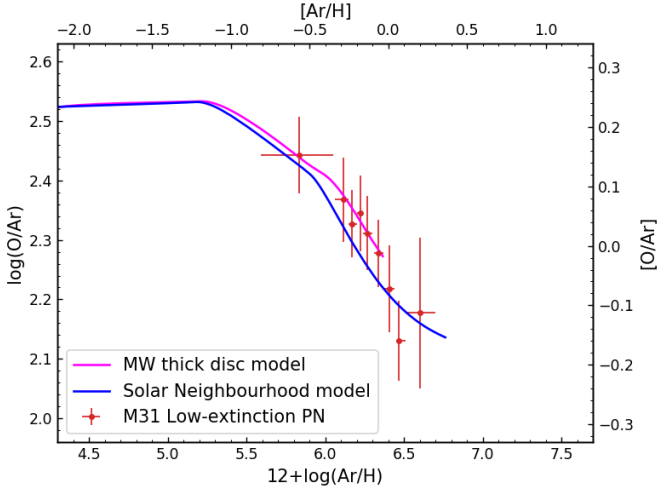
**Notes.** Listed values include standard deviation of  $\log(\text{O}/\text{Ar})$  in each bin, error on mean  $\log(\text{O}/\text{Ar})$  values and mean measurement error in each bin.

Fig. 2 we show the resulting mean  $\log(\text{O}/\text{Ar})$  values in bins of  $12 + \log(\text{Ar}/\text{H})$  with the adopted error bars.

The distribution in the right panel of Fig. 2 is clearly a function of argon abundance, with the highest  $\log(\text{O}/\text{Ar})$  values ( $\approx 2.5$ ) at the lowest measured argon abundance ( $12 + \log(\text{Ar}/\text{H}) \approx 6.0$ ) and the lowest mean  $\log(\text{O}/\text{Ar})$  measured value ( $\approx 2.08$ ) for the most argon abundant ( $12 + \log(\text{Ar}/\text{H}) \approx 7.5$ ) bin, for the high extinction PNe. We also show the clipped outlier PNe individually. They are few in number and do not affect the general trend.

### 3.2. Tracing chemical enrichment in the old disc with PN abundances

We now focus on the distribution of, and trend in, the mean  $\log(\text{O}/\text{Ar})$  values versus  $12 + \log(\text{Ar}/\text{H})$  for the low-extinction PNe, which trace the early evolution. In Fig. 3, their values are compared with the evolution tracks for oxygen and argon for the MW thick and thin discs (Kobayashi et al. 2020a). According



**Fig. 3.**  $\log(\text{O}/\text{Ar})$  values for the low-extinction PNe in M31 binned as a function of their  $12 + \log(\text{Ar}/\text{H})$  values and shown as red symbols; for each bin the mean  $\log(\text{O}/\text{Ar})$  is plotted along with the sigma-clipped error. The continuum lines reproduce the chemical evolution tracks for the oxygen and argon elements modelled by Kobayashi et al. (2020a) for the MW thick disc (magenta) and the solar neighbourhood (dark blue). The  $[\text{Ar}/\text{H}]$  abundances and  $[\text{O}/\text{Ar}]$  ratios with respect to the solar values ( $12 + \log(\text{Ar}/\text{H})_{\odot} = 6.38$  and  $\log(\text{O}/\text{Ar})_{\odot} = 2.29$ ) are marked on the top and right axes, respectively.

to these models, argon is made in both Type II and Ia supernovae, with a greater fraction in supernovae II than for Fe and a smaller fraction than for oxygen. Therefore, the decrease in the  $\log(\text{O}/\text{Ar})$  versus  $12 + \log(\text{Ar}/\text{H})$  plane would signal an increase in the Type Ia supernova contribution, which is indeed shown by the models. In the solar neighbourhood, 34% of Ar is produced from Type Ia supernovae (see Kobayashi et al. 2020a). Interestingly, the Kobayashi et al. (2020a) model tracks for MW thin and thick discs show two knees: the second knee, at  $[\text{Ar}/\text{H}] = -0.5$ , is caused by the contribution of Type Ia supernovae, similarly to that seen in  $[\alpha/\text{Fe}]$  versus  $[\text{Fe}/\text{H}]$  plots as in Hayden et al. (2015), while the knee at  $[\text{Ar}/\text{H}] = -1.2$  is caused by the dependence of argon production on the metallicity of core collapsed Type II supernovae.

We first compare the  $\log(\text{O}/\text{Ar})$  versus  $12 + \log(\text{Ar}/\text{H})$  binned distribution for low-extinction PNe with the chemical evolution models. The O and Ar abundance distributions of the M31 low-extinction disc PNe show a possible slightly positive and null (within the errors) radial gradient, respectively (see Paper IV). In turn, the  $\log(\text{O}/\text{Ar})$  distribution has a near constant average values and similar large scatter over the entire 2–30 kpc range (see Sect. 2.4, Fig. 1, and Table 1). The measured null radial abundance gradients for the low-extinction PNe and the large and constant scatter across the entire radial range supports the view that their distribution in the  $\log(\text{O}/\text{Ar})$  versus  $12 + \log(\text{Ar}/\text{H})$  plane is the result of an effective radial mixing of different chemical enrichment tracks over the 2–30 kpc radial range. Significant radial mixing of the old stellar population over the entire Panchromatic *Hubble* Andromeda Treasury (PHAT) survey area was also reported by Williams et al. (2017).

In Fig. 3, the comparison of the  $\log(\text{O}/\text{Ar})$  versus  $12 + \log(\text{Ar}/\text{H})$  binned distribution for low-extinction PNe with the Kobayashi et al. (2020a) models shows that the highest  $\log(\text{O}/\text{Ar})$  at low  $12 + \log(\text{Ar}/\text{H})$  values for M31 disc low-extinction PNe are representative of the stellar population that forms soon after  $\alpha$  elements are produced in core collapse super-

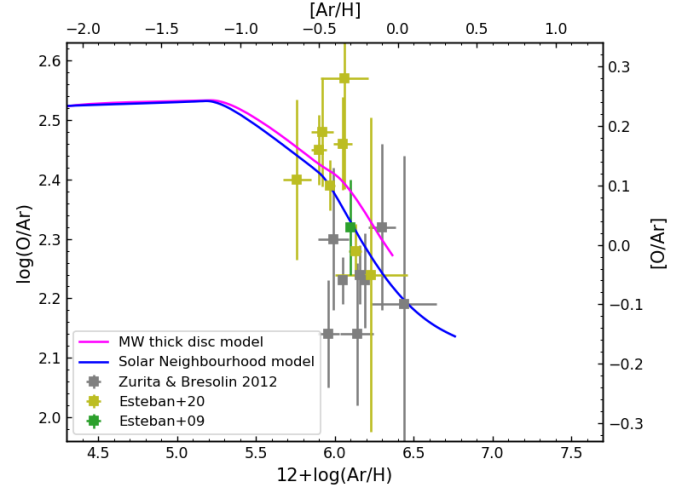


**Fig. 4.** Same as Fig. 3 but showing the M31 HII region  $\log(\text{O}/\text{Ar})$  values as a function of their  $12 + \log(\text{Ar}/\text{H})$  together with the chemical evolution tracks of Kobayashi et al. (2020a). The  $[\text{Ar}/\text{H}]$  ratios with respect to the solar values are marked on the top and right axes, respectively.

novae, from short-lived massive stars. After Type Ia supernovae start producing additional argon relative to oxygen, the ISM is enriched and stars subsequently form with decreasing  $\log(\text{O}/\text{Ar})$  values at increasing argon abundance ( $12 + \log(\text{Ar}/\text{H})$ ). The same chemical evolution models, following the aforementioned processes, also show the decreasing trends in the analogous  $[\alpha/\text{Fe}]$  versus  $[\text{Fe}/\text{H}]$  plot for stellar abundances, as seen for the MW (see e.g., Hayden et al. 2015).

In the MW (also recently in UGC 10738; Scott et al. 2021), it was found that the thick disc is more metal-poor and  $\alpha$ -enriched compared to the thin disc, occupying distinct regions of the  $[\alpha/\text{Fe}]$  versus  $[\text{Fe}/\text{H}]$  plot (see e.g., Hayden et al. 2015; Kobayashi et al. 2020a). The explanation for the  $\alpha$  enhancement in the MW thick disc is that it has had a faster chemical enrichment timescale than the MW thin disc, with high star formation efficiency in the thick disc at early times, while the extended star formation in the MW thin disc generates higher iron abundance values than those in the MW thick disc. Figure 3 shows that correspondingly the MW thin disc also reaches higher Ar abundances than the thick disc. On the contrary, unlike the MW thick disc, the 4.5 Gyr and older thicker disc in M31 reaches higher argon abundances than the MW thick disc and as high as those reached by the extended star formation in the solar neighbourhood.

### 3.3. Fresh infall of gas: Oxygen and argon abundances of HII regions in the M31 disc

A useful insight on the chemical evolution of the M31 discs is given by the properties of the younger generation of stars with respect to the older low-extinction PNe in the M31 thicker disc. We thus explore the  $\log(\text{O}/\text{Ar})$  versus  $12 + \log(\text{Ar}/\text{H})$  distribution (Fig. 4) measured for the HII regions in the M31 thin disc (see Sect. 2.4). Similar to the M31 PNe, the HII regions follow a decreasing trend in  $\log(\text{O}/\text{Ar})$  with  $12 + \log(\text{Ar}/\text{H})$  with a significant scatter. When we compare the HII region  $\log(\text{O}/\text{Ar})$  distribution with the MW thick/thin chemical enrichment models, we see that the HII region values do not cluster near the end of the track for the MW thin disc, at high  $[\text{Ar}/\text{H}]$  values. At a

given argon abundance, their large scatter supports the hypothesis that their distribution in the  $\log(\text{O}/\text{Ar})$  versus  $12 + \log(\text{Ar}/\text{H})$  plane is due to differences in present-day abundances. The range of  $\log(\text{O}/\text{Ar})$  values, between 2.15 to 2.6, at argon abundance  $12 + \log(\text{Ar}/\text{H}) \approx 6.0$  indicates spatial variations of the abundances in the M31 gas phase of the thin disc, due to different degree of mixing of metal-poor gas with the enriched ISM in the disc, and also with the starburst in the 10–17 kpc region (Kang et al. 2009). The spatial variations are plausibly linked with the recent production of oxygen in the starburst and rainfall of gas over the M31 disc, which may be related to the extra planar HI gas (Westmeier et al. 2008).

### 3.4. Constraints on the chemical enrichment of the thin disc in M31 with PN abundances

In this section we investigate the differences in the chemical enrichment of the high-extinction PNe in M31, which are tracing the kinematically thin disc of M31 (Paper II), with respect to the low-extinction older PNe. We note that high-extinction PNe occupy regions of the  $\log(\text{O}/\text{Ar})$  versus  $12 + \log(\text{Ar}/\text{H})$  plane that, even if with some overlaps, are somewhat different from the low-extinction PNe (see Fig. 2, right plot). We find that the decrease for the mean  $\log(\text{O}/\text{Ar})$  versus  $12 + \log(\text{Ar}/\text{H})$  is linear for the low-extinction PNe. The mean  $\log(\text{O}/\text{Ar})$  versus  $12 + \log(\text{Ar}/\text{H})$  for the high-extinction PNe are larger than those for the low extinction PNe in most bins, but for the  $12 + \log(\text{Ar}/\text{H}) = 6.1\text{--}6.3$  range (3 bins), where they are lower.

We compare the linear fit to the mean  $\log(\text{O}/\text{Ar})$  values in the  $12 + \log(\text{Ar}/\text{H}) = 6\text{--}6.7$  range, for the high- and low-extinction PNe in the M31 disc, and validate them statistically. The high- and low-extinction PNe can be fitted by linear functions with a Bayesian information criterion<sup>4</sup> (BIC; Schwarz 1978) values of  $-50.42$  and  $-48.99$ , respectively. The linear fit to the low-extinction PNe (slope =  $-0.54 \pm 0.09$ ; intercept =  $5.7 \pm 0.58$ ) is the best fit (see Fig. 5), with higher-order functions not producing better fits (giving higher BIC values instead). A third-order polynomial does however provide a better fit to the high-extinction PNe (BIC =  $-56.17$ ) as shown in Fig. 5, thus validating the deviation from simple linear decrease.

If both the high- and low-extinction PNe were following the same enrichment history, the high-extinction PNe, which have an age of  $\sim 2.5$  Gyr or younger (Paper II), should populate low  $\log(\text{O}/\text{Ar})$ - higher argon abundances region of the evolutionary track (see Sects. 3.2 and 3.3). The existence of high-extinction younger PNe with high  $\log(\text{O}/\text{Ar})$  values at relative lower argon abundances support a secondary infall event with less chemically evolved gas.

## 4. Constraints on chemical evolution and the formation history of the M31 disc

As illustrated in Sect. 3, galactic chemical evolution (GCE) models of the MW thick disc and solar neighbourhood (Kobayashi et al. 2020a) have a near linear decrease of  $\log(\text{Ar}/\text{O})$  values in the  $12 + \log(\text{Ar}/\text{H}) = 6\text{--}6.7$  range (see Fig. 3). Deviations from a simple linearly decreasing chemical evolution track may be related to either quenching or a secondary infall of gas onto a galaxy, which then causes a modification

<sup>4</sup> It is a criterion for model selection among a finite set of models based on Bayesian statistics. Overfitting may result from adding parameters to increase the likelihood of a function. BIC introduces a penalty term for the number of parameters in the model in order to avoid overfitting.

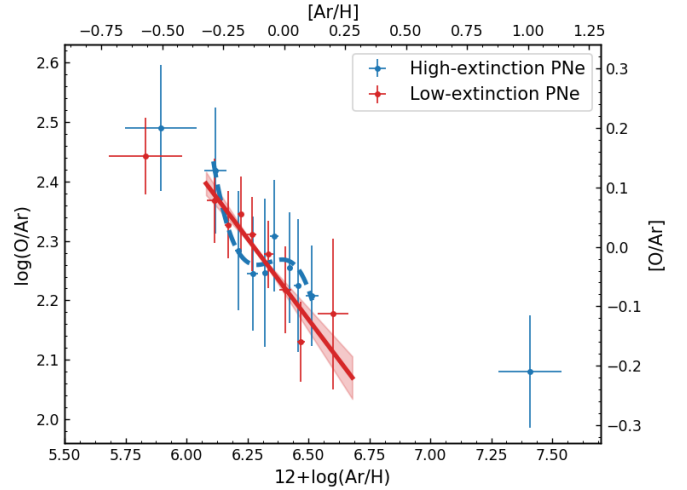


**Fig. 5.** Same as Fig. 3, showing the mean  $\log(\text{O}/\text{Ar})$  values of the high- (blue) and low- (red) extinction PNe but now also showing the linear fit with uncertainty shaded for the low-extinction sample. For the high-extinction PNe, the dashed blue line shows a third-order polynomial curve that better fits the lower mean  $\log(\text{O}/\text{Ar})$  values of the high-extinction PNe in the  $12 + \log(\text{Ar}/\text{H}) = 6.1\text{--}6.3$  range. The  $[\text{Ar}/\text{H}]$  abundances and  $[\text{O}/\text{Ar}]$  ratios with respect to the solar values are marked on the top and right axes, respectively.

of the ISM chemical abundances (see Sect. 4.2 for details and Matteucci 2021 for a review).

### 4.1. Regions of homogeneous chemical evolution in M31 discs

The chemical enrichment models do not include the effects of radial metallicity gradients. Therefore, as the high-extinction PNe have i) a steeper argon abundance gradient (Paper IV) and ii) have distinct behaviour of the  $\log(\text{O}/\text{Ar})$  values in three radial ranges, as described in Sect. 2.4, the steps prior to the chemical modelling include the identification of the disc regions with nearly flat  $\log(\text{O}/\text{Ar})$  radial gradients.

In Fig. 6 we show the distribution of the high-extinction PNe in the three radial ranges, inner disc ( $R_{\text{GC}} < 14$  kpc) [Left], starburst region ( $14 \leq R_{\text{GC}} \leq 18$  kpc) [Middle], and outer disc ( $R_{\text{GC}} > 18$  kpc) [Right], with respect to the low extinction PN values for the entire M31 disc. While in Sect. 3.4 the high extinction PNe have larger  $\log(\text{O}/\text{Ar})$  values than the low extinction PNe, we find that the high extinction, younger, PNe in the inner disc cluster towards the end, and below, the low extinction PNe distribution at relatively high  $[\text{Ar}/\text{H}]$  (see the left panel of Fig. 6). Considering their younger age, they are consistent with the chemical evolution only if also there is a dilution of the ISM by infall of metal-poorer gas. In the middle panel of Fig. 6, the high extinction PNe show a large range in argon abundances for a 2.5 Gyr and younger evolution. Those points on the top of the low-extinction PNe distribution may be consistent with the strong starburst located in this disc region (Kang et al. 2009) and a range of initial gas mixing. In the right panel of Fig. 6, the high  $\log(\text{O}/\text{Ar})$  values at relatively low argon abundances for the younger high extinction PNe, with respect to the low extinction PNe distribution, indicate a higher star formation efficiency in those outer regions, that is. shorter timescales in the thin disc with respect to the thicker disc, with the progenitor of these younger PNe being formed mostly out of the less enriched gas.

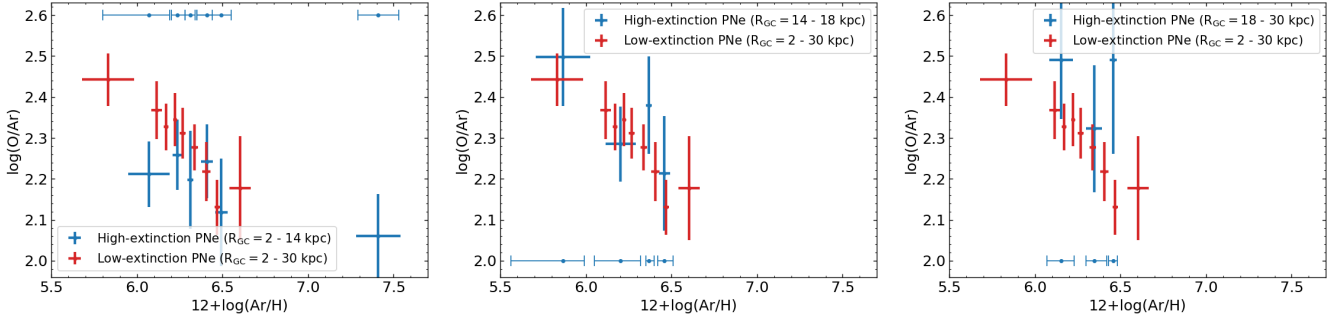


**Fig. 6.** Same as Fig. 3, showing the mean  $\log(\text{O}/\text{Ar})$  values of the high- (blue) and low- (red) extinction PNe, but now showing only high-extinction PNe in the inner disc ( $R_{\text{GC}} < 14$  kpc; left), in the starburst region ( $14 \leq R_{\text{GC}} \leq 18$  kpc; middle), and in the outer disc ( $R_{\text{GC}} > 18$  kpc; right). The blue error bars parallel to the  $x$  axis indicate the width of the bins in  $12 + \log(\text{A}/\text{H})$  for the high-extinction (blue) PN sub-samples in the different annuli.

#### 4.2. Imprint of a secondary gas inflow on the oxygen and argon abundances in the inner ( $R_{\text{GC}} < 14$ kpc) M31 thin disc from a chemical evolution model

To understand the chemical evolution of the younger disc in M31 within 14 kpc, we first review the arguments available in the literature used to describe the chemical evolution of the MW discs. Two infall-model scenarios were proposed to explain the distribution of the MW stars in the  $[\alpha/\text{Fe}]$  (or  $[\text{Mg}/\text{Fe}]$ ) versus  $[\text{Fe}/\text{H}]$  plane, in different radial ranges (see the models by Grisoni et al. 2017; Spitoni et al. 2019, 2021). According to these models, the MW thick disc stars form rapidly with high star formation efficiency, which leads to high  $[\alpha/\text{Fe}]$  values for its stars. Eventually star formation is suppressed as gas is depleted in the MW thick disc. After some time ( $t_{\text{max}}$ ), further infall of gas, either pristine or pre-enriched, occurs, which dilutes the available ISM and then triggers star formation, at a lower efficiency. This may lead to the formation of loops in the GCE tracks in the  $[\alpha/\text{Fe}]$  (or  $[\text{Mg}/\text{Fe}]$ ) versus  $[\text{Fe}/\text{H}]$  plane (Matteucci 2021). Thin disc stars in the MW are formed initially at a lower metallicity, which then increases with time. In the MW thin disc, stars have lower  $[\alpha/\text{Fe}]$  values than thick disc stars because of the diminished star formation efficiency. The time interval  $t_{\text{max}}$ , the amount of accreted gas, and whether the latter is pristine or pre-enriched, drives the extent of these loops in the GCE tracks. Larger loops can be present for larger  $t_{\text{max}}$  values (see Fig. 14 in Spitoni et al. 2019) and/or larger amount of pristine gas. The loop also becomes narrower if the infalling gas is pre-enriched (Spitoni et al. 2021).

As illustrated in Sects. 3 and 4.1, the oxygen and argon abundance distribution and ratios for young high extinction PNe support a secondary event of gas accretion. Hence, we constructed new, GCE models for the inner disc regions ( $R_{\text{GC}} < 14$  kpc) with two gas inflow phases for the M31 disc, using the same chemical evolution code by Kobayashi et al. (2020a). The models are constrained using the star formation history and metallicity distribution function (MDF) measured for the M31 disc within the PHAT footprint ( $R_{\text{GC}} \approx 18$  kpc) using isochrone fitting to the observed red giant branch (RGB) stars (Williams et al. 2017). A detailed illustration of these models is provided in Appendix B.

In these chemical evolution models, the thicker disc older stars are formed by the first gas inflow, with the infall timescale of 1 Gyr. The star formation rate of the first burst differs in the models though, with a weaker first burst by a factor  $\approx 2.5$  for the second model, which is still within the uncertainties of the total star formation rate versus age for the entire PHAT footprint (see Williams et al. 2017 and our Appendix B). The star formation rate ceases after 2 Gyr and 3 Gyr, in the fiducial and weaker first

burst model, respectively. The thin disc stars instead are formed by the second inflow, started at 9 Gyr with the infall timescale of 2 Gyr. In the two models, the star formation rate for the second burst differs at the 20% level, with the fiducial model having a relatively weak second burst. The chemical composition of both gas inflows is set to be primordial, which results in the loop in the  $\log(\text{O}/\text{Ar})$  versus  $12 + \log(\text{Ar}/\text{H})$  plane. The star formation timescales are 10 Gyr and 2 Gyr for the thicker and thin disc stars, respectively, which means that the star formation efficiency is five times higher during the thin disc formation than for the thicker disc. A small amount of gas outflow (with the timescale of 5 Gyr) is also included. These new models are shown in Fig. 7 together with the high extinction PN oxygen and argon measurements for the M31 ISM within 14 kpc, in the  $\log(\text{O}/\text{Ar})$  versus  $12 + \log(\text{Ar}/\text{H})$  plane, and the low extinction PNe  $\log(\text{O}/\text{Ar})$  versus  $12 + \log(\text{Ar}/\text{H})$  measurements over the entire disc. The list of the relevant parameters for the chemical evolution models is given in Table B.1.

We discuss the two chemical enrichment tracks in turn. In Fig. 7 [Left], the fiducial model described in Appendix B reaches  $12 + \log(\text{Ar}/\text{H}) \sim 7.25$  at lookback time  $\sim 5$  Gyr ago, following which the star formation is suppressed in the thick disc. Infall of primordial gas occurs  $\sim 5$  Gyr ago; it rapidly reduces the mean  $12 + \log(\text{Ar}/\text{H})$  value of the ISM and leads to a second burst of star-formation. At the start of the second burst of star formation, prior to supernovae Type-Ia eruption, the  $\log(\text{O}/\text{Ar})$  value at corresponding lower metallicity increases, thereby producing the rising part of the loop (Fig. 7-[Left]). The loop turns over once the supernovae Type-Ia eruption kicks in, leading to a decrease of the  $\log(\text{O}/\text{Ar})$  value with increasing  $12 + \log(\text{Ar}/\text{H})$ , over the past  $\sim 4$  Gyr. The track reaches  $12 + \log(\text{Ar}/\text{H})$  values  $\approx 7.2$  at present times. The high argon abundance high extinction PNe are better reproduced by this fiducial model.

In Fig. 7 [Right], because of the weaker first star formation, the second model reaches  $12 + \log(\text{Ar}/\text{H}) \sim 6.7$  at lookback time  $\sim 5$  Gyr ago. With the dilution and loop following a similar pattern as for the model in the left panel, the track reaches  $12 + \log(\text{Ar}/\text{H})$  values  $\approx 6.7$  at present times. This chemical evolution model of the ISM in the M31 thin and thicker disc is in good agreement with the values traced by the low-extinction PNe and the loop covers the distribution of the high extinction PNe  $\log(\text{O}/\text{Ar})$  and  $12 + \log(\text{Ar}/\text{H})$  values at  $R_{\text{GC}} < 14$  kpc. However, super-solar metallicity values traced by the high-extinction PNe are not reached in this model, and the model seems to underestimate the amount of low-metallicity gas added. Such remaining discrepancies may be addressed in a future investigation with more extended chemo-dynamical modelling.

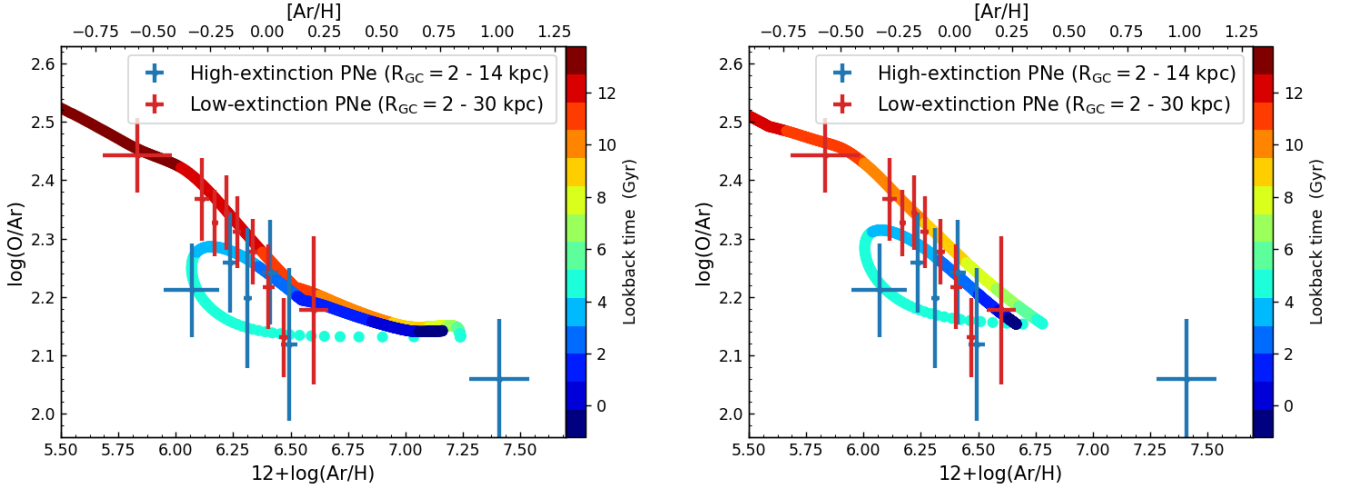


**Fig. 7.** Mean  $\log(\text{O}/\text{Ar})$  values of the low-extinction PNe (red) over the 2–30 kpc radial range, the high-extinction PNe (blue) within  $R_{\text{GC}} < 14$  kpc, and the new two-infall chemical evolution model for the M31 disc (see Sect. 4.2 for details), coloured by lookback time: the fiducial model on the left and the alternative model with a weaker first star formation on the right. The  $[\text{Ar}/\text{H}]$  abundances with respect to the solar values are marked on the top and right axes, respectively. More details on the chemical evolution models are provided in Appendix B.

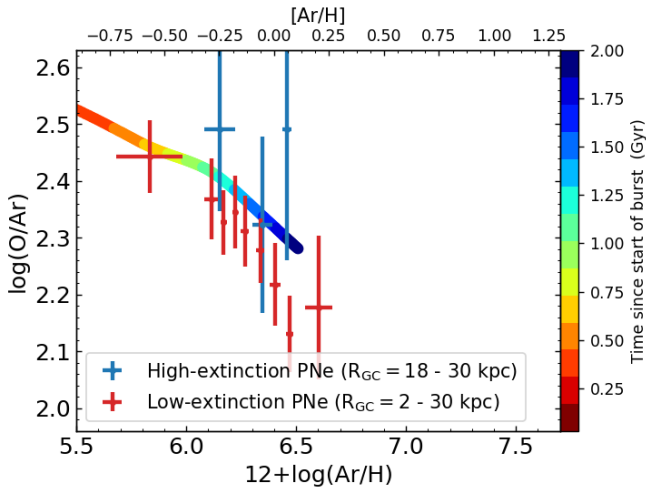


**Fig. 8.** Mean  $\log(\text{O}/\text{Ar})$  values of the low-extinction (red) PNe over the 2–30 kpc radial range and the high-extinction (blue) PNe in the outer disc  $R_{\text{GC}} > 18$  kpc. The chemical evolution track shows the chemical enrichment within approximately 2 Gyr following a burst of star formation. More details are provided in Appendix B.

In Fig. 8 we show the chemical evolution enrichment track computed with reference to a burst of star formation from a gas infall with primordial composition and a timescale of 2 Gyr to reproduce the chemical enrichment of the thin outer disc, at  $R_{\text{GC}} > 18$  kpc. The lookback time shows the time from the start of the gas infall. The adopted timescale is even shorter than that of the MW thick disc, and it is as short as for nearby early-type galaxies. It clearly illustrates the shorter star formation timescale and the lower argon abundance of the outer thin disc in M31.

## 5. Possible gas content of the merging satellite in the M31 disc

From the AVD relation in the 14–17 kpc and 17–20 kpc, in Paper II we constrained the baryonic mass of the satellite that

merged with the M31 disc. The estimated merger mass ratio from the AVD relation is 1 : 5 (Hopkins et al. 2008, 2009), hence the baryonic mass of the satellite  $M_{\text{sat}} = 1.4 \times 10^{10} M_{\odot}$ . Adopting the best-fit galaxy gas-fraction to galaxy stellar mass relation (Díaz-García & Knapen 2020), the estimated gas fraction for the satellite would then be  $\sim 19\%$ , with a total mass in gas of  $M_{\text{HI,sat}} = 2.8 \times 10^9 M_{\odot}$ . We can compare the estimated gas mass brought in from the satellite with the i) mass in stars formed during the last 4.5 Gyr and ii) the amount of neutral HI still detected in the M31 disc.

Williams et al. (2017) found that the total stellar mass produced over the last  $\sim 2$  Gyr in the M31 disc is  $M_{\text{stellar}} \sim 4.5 \times 10^9 M_{\odot}$ , and the present-day total mass of HI gas in the M31 disc is  $M_{\text{HI}} = 4.23 \times 10^9 M_{\odot}$  (Chemin et al. 2009). Thus, prior to the burst of star formation  $\sim 2.5$  Gyr ago (Bernard et al. 2015; Williams et al. 2017), a gas mass of  $M_{\text{gas},2\text{Gyr}} \approx 9 \times 10^9 M_{\odot}$  must have been available in the M31 disc. This amount is much larger than the estimated amount brought in by the merging satellite. Thus, residual gas had to still be present in the pre-merger M31 disc, which was then diluted by  $\Delta[\text{Ar}/\text{H}] \approx -0.5$  dex as observed in the argon abundance distribution. The high extinction PNe were formed out of this diluted ISM within 14 kpc, as illustrated in Fig. 7, and mostly from satellite gas at  $R_{\text{GC}} > 18$  kpc (see Fig. 8).

From the mass-metallicity relation (e.g., Zahid et al. 2017), the gas from the merging satellite galaxy would be pre-enriched, but at lower metallicity values than the ISM of the M31 pre-merger disc. A galaxy of mass equal to  $M_{\text{sat}}$  is expected to have a metallicity  $\sim -0.5$  dex. The MDF of the RGB stars in the GSS from Conn et al. (2016), and Cohen et al. (2018) provide evidence for a metal-poor population of stars with  $[\text{Fe}/\text{H}]$  in the range  $[-1.0; -0.2]$  dex. Then a second infall of gas related to the wet merger of the satellite onto the M31 disc would dilute the previously enriched ISM in the M31 pre-merger disc. The starburst triggered by the newly acquired gas would reproduce the lower  $[\text{Ar}/\text{H}]$  values and the  $\log(\text{O}/\text{Ar})$  distribution of the high-extinction PNe, as discussed in Sect. 4.2. The lower metallicity of the gas in the satellite, estimated either from the mass-metallicity relation or the observation of the GSS stars, is consistent with extent of the ‘loop’ towards lower  $[\text{Ar}/\text{H}]$  abundances in the chemical evolution models shown in Fig. 7.

## 6. Conclusions

We have used the largest sample of PNe in the M31 disc with oxygen and argon measurements from Paper IV, as well as archival measurements of these elements for HII regions. We have compared their distributions with chemical evolution models for the MW thick disc and the solar neighbourhood and with chemical enrichment models for the M31 discs with secondary infall phases. Our main conclusions are that the  $\log(\text{O}/\text{Ar})$  versus argon abundance distributions of the nebular emissions of the stellar evolution phases (e.g., HII regions and PNe) are valid alternatives to the  $[\alpha/\text{Fe}]$  versus  $[\text{Fe}/\text{H}]$  diagrams that have been widely used to constrain the star formation efficiency in the MW. By using this new approach, we determined a different chemical evolution history for the thin and thicker discs in the Andromeda galaxy, with the thin disc in M31 having been affected by a wet merger. Our conclusions can be further illustrated as follows:

- The oxygen-to-argon ratio,  $\log(\text{O}/\text{Ar})$ , values of PNe are high at low argon abundances and monotonically decrease to lower values at higher argon abundances, consistent with predictions of the ISM properties from GCE models. This is the first vivid example that galactic chemical enrichment is imprinted in the  $\log(\text{O}/\text{Ar})$  versus Ar plane.
- The  $\log(\text{O}/\text{Ar})$  versus argon abundance distribution for the low-extinction, 4.5 Gyr and older, PNe associated with the M31 thicker disc supports a chemical evolution where the thicker disc forms from infalling gas with a primordial composition at early times and reaches a high argon abundance similar to that of the solar neighbourhood in the MW ( $12 + \log(\text{Ar}/\text{H}) \approx 6.7$ ).
- The  $\log(\text{O}/\text{Ar})$  versus  $12 + \log(\text{Ar}/\text{H})$  distribution for the high-extinction, 2.5 Gyr and younger, PNe associated with the thin disc of M31 overlaps with that of the low-extinction PNe, with quantifiable differences. Three regions are identified in the M31 disc: inner disc, starburst region, and outer disc.
- In the inner disc ( $R_{\text{GC}} < 14$  kpc), the high-extinction, 2.5 Gyr and younger, PNe form after a secondary event with infall of metal-poor gas that mixed with the pre-enriched ISM in the pre-merger M31 disc. This is in agreement with the two-infall GCE model described in Sect. 4.2 and Appendix B. In the starburst region ( $14 \leq R_{\text{GC}} \leq 18$  kpc), the high-extinction, 2.5 Gyr and younger, PNe display a range of initial gas mixing and high  $\log(\text{O}/\text{Ar})$  values, consistent with the strong starburst located in this region of the M31 disc (see Kang et al. 2009). In the  $R_{\text{GC}} > 18$  outer disc, the high-extinction PNe progeny are formed mostly in a burst of star formation that occurred  $\approx 2$  Gyr ago from less chemically enriched satellite gas.
- The  $\log(\text{O}/\text{Ar})$  versus  $12 + \log(\text{Ar}/\text{H})$  distribution for the HII regions in M31 has a large scatter at fixed argon abundance  $12 + \log(\text{Ar}/\text{H}) \approx 6.2$ . This spread is consistent with spatial variations and different degrees of mixing, which is reasonably linked to current rainfall of metal-poor gas from extra-planar HI, part of which may have also originated from the satellite.
- In contrast to the chemical enrichment history and structure of the thin disc in the MW, the thin disc in M31 is less radially extended, formed stars more recently and at a higher star formation efficiency, and had a faster chemical enrichment timescale than the thicker disc in M31.

The next steps of this investigation will explore the kinematical and chemical abundance properties of the PNe associated with the substructures in the outer disc and inner halo of M31.

**Acknowledgements.** MAR and SB thank the European Southern Observatory (ESO), Garching, Germany for supporting SB's visit through the 2021 ESO SSDF. MAR, SB and OG are grateful for the hospitality of the Mount Stromlo Observatory and the Australian National University (ANU). MAR and OG thank the Research School of Astronomy and Astrophysics at ANU for support through their Distinguished Visitor Program. This work was supported by the DAAD under the Australia-Germany joint research program with funds from the German Federal Ministry for Education and Research. SB is funded by the INSPIRE Faculty award (DST/INSPIRE/04/2020/002224), Department of Science and Technology (DST), Government of India. CK acknowledge funding from the UK Science and Technology Facility Council through grant ST/R000905/1 and ST/V000632/1. Based on observations obtained at the MMT Observatory, a joint facility of the Smithsonian Institution and the University of Arizona. Based on observations obtained with MegaPrime/MegaCam, a joint project of CFHT and CEA/DAPNIA, at the Canada-France-Hawaii Telescope (CFHT). This research made use of Astropy—a community-developed core Python package for Astronomy (Astropy Collaboration 2013), SciPy (Virtanen et al. 2020), NumPy (Oliphant 2015) and Matplotlib (Hunter 2007). This research also made use of NASA's Astrophysics Data System (ADS <https://ui.adsabs.harvard.edu>).

## References

- Aniyan, S., Freeman, K. C., Arnaboldi, M., et al. 2018, *MNRAS*, 476, 1909
- Aniyan, S., Ponomareva, A. A., Freeman, K. C., et al. 2021, *MNRAS*, 500, 3579
- Astropy Collaboration (Robitaille, T. P., et al.) 2013, *A&A*, 558, A33
- Belokurov, V., Erkal, D., Evans, N. W., Koposov, S. E., & Deason, A. J. 2018, *MNRAS*, 478, 611
- Belokurov, V., Sanders, J. L., Fattahi, A., et al. 2020, *MNRAS*, 494, 3880
- Bernard, E. J., Ferguson, A. M. N., Richardson, J. C., et al. 2015, *MNRAS*, 446, 2789
- Bhattacharya, S., Arnaboldi, M., Caldwell, N., et al. 2019a, *A&A*, 631, A56 (Paper I)
- Bhattacharya, S., Arnaboldi, M., Hartke, J., et al. 2019b, *A&A*, 624, A132 (Paper II)
- Bhattacharya, S., Arnaboldi, M., Gerhard, O., et al. 2021, *A&A*, 647, A130 (Paper III)
- Bhattacharya, S., Arnaboldi, M., Caldwell, N., et al. 2022, *MNRAS*, submitted, [arXiv:2203.06428] (Paper IV)
- Bland-Hawthorn, J., & Gerhard, O. 2016, *ARA&A*, 54, 529
- Chemin, L., Carignan, C., & Foster, T. 2009, *ApJ*, 705, 1395
- Chiappini, C., Matteucci, F., & Gratton, R. 1997, *ApJ*, 477, 765
- Cohen, R. E., Kalirai, J. S., Gilbert, K. M., et al. 2018, *AJ*, 156, 230
- Comerón, S., Salo, H., Knapen, J. H., & Peletier, R. F. 2019, *A&A*, 623, A89
- Conn, A. R., McMonigal, B., Bate, N. F., et al. 2016, *MNRAS*, 458, 3282
- Cortesi, A., Arnaboldi, M., Coccato, L., et al. 2013, *A&A*, 549, A115
- Delgado-Inglada, G., Morisset, C., & Stasińska, G. 2014, *MNRAS*, 440, 536
- Delgado-Inglada, G., Rodríguez, M., Peimbert, M., Stasińska, G., & Morisset, C. 2015, *MNRAS*, 449, 1797
- Díaz-García, S., & Knapen, J. H. 2020, *A&A*, 635, A197
- Dorman, C. E., Guhathakurta, P., Seth, A. C., et al. 2015, *ApJ*, 803, 24
- D'Souza, R., & Bell, E. F. 2018, *MNRAS*, 474, 5300
- Esteban, C., Bresolin, F., Peimbert, M., et al. 2009, *ApJ*, 700, 654
- Esteban, C., Bresolin, F., García-Rojas, J., & Toribio San Cipriano, L. 2020, *MNRAS*, 491, 2137
- Fabricant, D., Fata, R., Roll, J., et al. 2005, *PASP*, 117, 1411
- García-Hernández, D. A., & Górný, S. K. 2014, *A&A*, 567, A12
- García-Hernández, D. A., Ventura, P., Delgado-Inglada, G., et al. 2016, *MNRAS*, 458, L118
- Gilmore, G., & Reid, N. 1983, *MNRAS*, 202, 1025
- Grisoni, V., Spitoni, E., Matteucci, F., et al. 2017, *MNRAS*, 472, 3637
- Hammer, F., Yang, Y. B., Wang, J. L., et al. 2018, *MNRAS*, 475, 2754
- Hartke, J., Arnaboldi, M., Gerhard, O., et al. 2022, *A&A*, 663, A12
- Hayden, M. R., Bovy, J., Holtzman, J. A., et al. 2015, *ApJ*, 808, 132
- Haywood, M., Di Matteo, P., Lehnert, M. D., Katz, D., & Gómez, A. 2013, *A&A*, 560, A109
- Helmi, A., Babusiaux, C., Koppelman, H. H., et al. 2018, *Nature*, 563, 85
- Hopkins, P. F., Cox, T. J., Younger, J. D., & Hernquist, L. 2009, *ApJ*, 691, 1168
- Hopkins, P. F., Hernquist, L., Cox, T. J., Younger, J. D., & Besla, G. 2008, *ApJ*, 688, 757
- Hunter, J. D. 2007, *Comput. Sci. Eng.*, 9, 90
- Ibata, R., Irwin, M., Lewis, G., Ferguson, A. M. N., & Tanvir, N. 2001, *Nature*, 412, 49
- Kang, Y., Bianchi, L., & Rey, S.-C. 2009, *ApJ*, 703, 614
- Kobayashi, C., & Nakasato, N. 2011, *ApJ*, 729, 16
- Kobayashi, C., & Nomoto, K. 2009, *ApJ*, 707, 1466
- Kobayashi, C., Karakas, A. I., & Lugaro, M. 2020a, *ApJ*, 900, 179

- Kobayashi, C., Leung, S.-C., & Nomoto, K. 2020b, *ApJ*, 895, 138
- Kwitter, K. B., & Henry, R. B. C. 2022, *PASP*, 134, 022001
- Kwitter, K. B., Lehman, E. M. M., Balick, B., & Henry, R. B. C. 2012, *ApJ*, 753, 12
- Maciel, W. J., & Koppen, J. 1994, *A&A*, 282, 436
- Magrini, L., Coccato, L., Stanghellini, L., Casasola, V., & Galli, D. 2016, *A&A*, 588, A91
- Matteucci, F. 2021, *A&ARv*, 29, 5
- McConnachie, A. W., Irwin, M. J., Ibata, R. A., et al. 2009, *Nature*, 461, 66
- McConnachie, A. W., Ibata, R., Martin, N., et al. 2018, *ApJ*, 868, 55
- Monachesi, A., Gómez, F. A., Grand, R. J. J., et al. 2019, *MNRAS*, 485, 2589
- Nomoto, K., Kobayashi, C., & Tominaga, N. 2013, *ARA&A*, 51, 457
- Oliphant, T. E. 2015, *Guide to NumPy*, 2nd edn. (USA: CreateSpace Independent Publishing Platform)
- Peña, M., & Flores-Durán, S. N. 2019, *Rev. Mex. Astron. Astrofis.*, 55, 255
- Pulsoni, C., Gerhard, O., Arnaboldi, M., et al. 2018, *A&A*, 618, A94
- Quinn, P. J., & Goodman, J. 1986, *ApJ*, 309, 472
- Sanders, N. E., Caldwell, N., McDowell, J., & Harding, P. 2012, *ApJ*, 758, 133
- Schwarz, G. 1978, *Ann. Stat.*, 6, 461
- Scott, N., van de Sande, J., Sharma, S., et al. 2021, *ApJ*, 913, L11
- Sellwood, J. A. 2014, *Rev. Mod. Phys.*, 86, 1
- Spitoni, E., Silva Aguirre, V., Matteucci, F., Calura, F., & Grisoni, V. 2019, *A&A*, 623, A60
- Spitoni, E., Verma, K., Silva Aguirre, V., et al. 2021, *A&A*, 647, A73
- Stanghellini, L., & Haywood, M. 2018, *ApJ*, 862, 45
- Ventura, P., Stanghellini, L., Dell’Agli, F., & García-Hernández, D. A. 2017, *MNRAS*, 471, 4648
- Virtanen, P., Gommers, R., Oliphant, T. E., et al. 2020, *Nat. Methods*, 17, 261
- Westmeier, T., Brüns, C., & Kerp, J. 2008, *MNRAS*, 390, 1691
- Williams, B. F., Dolphin, A. E., Dalcanton, J. J., et al. 2017, *ApJ*, 846, 145
- Wisnioski, E., Förster Schreiber, N. M., Wuyts, S., et al. 2015, *ApJ*, 799, 209
- Yoachim, P., & Dalcanton, J. J. 2006, *AJ*, 131, 226
- Yoachim, P., & Dalcanton, J. J. 2008, *ApJ*, 683, 707
- Zahid, H. J., Kudritzki, R.-P., Conroy, C., Andrews, B., & Ho, I. T. 2017, *ApJ*, 847, 18
- Zurita, A., & Bresolin, F. 2012, *MNRAS*, 427, 1463

## Appendix A: AGB evolution and possible dependences of PN oxygen and argon abundances on progenitor mass and metallicity

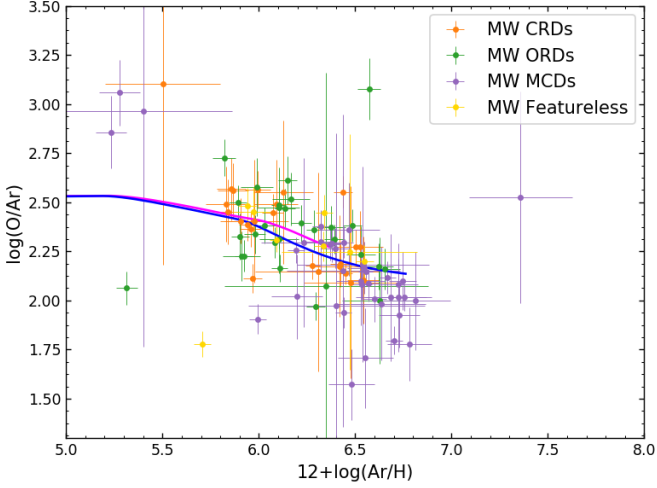


**Fig. A.1.**  $\log(\text{O}/\text{Ar})$  versus  $12 + \log(\text{Ar}/\text{H})$  distribution of 101 MW PNe marked by their circumstellar dust types from Ventura et al. (2017). The chemical evolution model tracks for the MW are the same as in Fig. 3.

Measured argon abundances in PNe reflect the ISM abundance at the time of their birth as surface argon is invariant during AGB evolution (Delgado-Inglada et al. 2015; García-Hernández et al. 2016). However, surface oxygen has been found to be modified in the AGB phase, particularly in stars with initial mass  $\geq 3M_{\odot}$  where HBB may result in an oxygen depletion of up to  $\sim 0.2$  dex (e.g. García-Hernández et al. 2016; Ventura et al. 2017). This results in measured PN oxygen abundances lower than their birth values. On the other hand, for PNe evolving from stars with initial masses of  $1 - 2M_{\odot}$  and  $Z < 0.008$ , TDU effects may result in an oxygen enrichment of up to  $\sim 0.3$  dex (e.g. García-Hernández et al. 2016; Ventura et al. 2017).

In a small sample of 20 MW PNe, Delgado-Inglada et al. (2015) had found that oxygen is enriched by up to  $\sim 0.3$  dex for intermediate metallicities of  $12 + \log(\text{O}/\text{H}) = 8.2 - 8.7$  for PNe with carbon-rich (circumstellar) dust (CRD), while it is invariant in PNe with oxygen-rich (circumstellar) dust (ORD). In Paper IV (see their Appendix D for a detailed discussion), using a larger sample of 101 MW PNe with abundance measurements and dust characterisation compiled by Ventura et al. (2017) compared to the chemical evolution tracks by Kobayashi et al. (2020a), we found that both CRD and ORD PNe (as well as PNe with featureless dust) follow the MW stellar evolution tracks with no oxygen enrichment or depletion relative to argon abundances. The same can be seen in Fig. A.1. However, as also noted Paper IV, many of the MW PNe with mixed chemistry dust (MCD) that are metal-rich ( $12 + \log(\text{Ar}/\text{H}) > 6.3$ ) preferentially have  $\log(\text{O}/\text{Ar})$  values below the model tracks, indicating lower oxygen or oxygen depletion. These MCD PNe are the youngest ( $< 300$  Myr) most metal-rich PNe in the MW sample (García-Hernández & Górny 2014).

As such young PNe are expected to exhibit enhanced nitrogen abundances based on the AGB evolution models of their progenitors (García-Hernández & Górny 2014; Ventura et al. 2017), we can check whether any M31 PN has enhanced nitrogen as further indication of a very young age and oxygen depletion, if any.

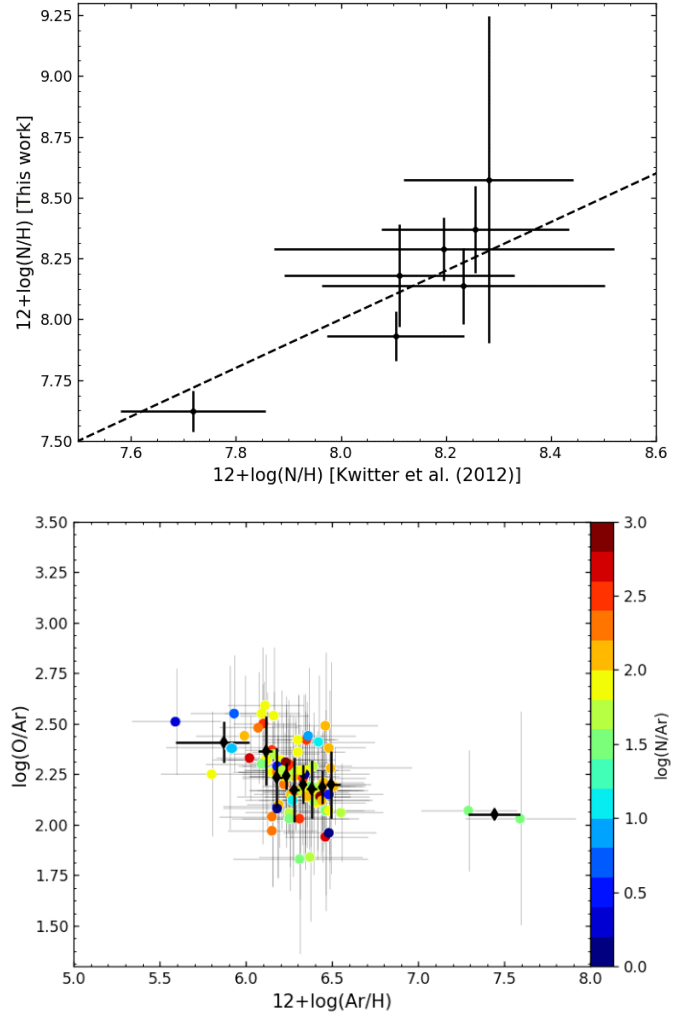


**Fig. A.2.** Nitrogen abundances and oxygen to argon ratios for M31 disc PNe. *Top:* Nitrogen abundance measurements compared for seven M31 disc PNe between Kwitter & Henry (2022) and this work. *Bottom:*  $\log(\text{O}/\text{Ar})$  versus  $12 + \log(\text{Ar}/\text{H})$  distribution of 91 M31 disc PNe coloured by their  $\log(\text{N}/\text{Ar})$  values. Measurement uncertainties are shown in grey. The PNe are binned as a function of their  $12 + \log(\text{Ar}/\text{H})$  values. For each bin the mean  $\log(\text{O}/\text{Ar})$  is plotted as black diamonds, and the error bar shows their standard deviation.

We measured nitrogen ionic abundances from the  $[\text{NII}] 6548,6584 \text{ \AA}$  line fluxes for a sub-sample of 87 M31 disc PNe that were observed in 2018 and 2019 with Hectospec at the MMT. The nitrogen elemental abundance is obtained by using the ionization correction factor (ICF) from Delgado-Inglada et al. (2014) (the nitrogen abundances for the full sample will be presented in a future publication). The nitrogen abundances for 7 PNe in the M31 disc are also measured by Kwitter et al. (2012) using Cloudy photoionisation models, independent of ICF. The top panel of Fig. A.2 shows that the nitrogen abundance measurements of the seven PNe derived here are consistent with those of Kwitter et al. (2012), indicating that the nitrogen abundance measurements are not strongly dependent on the adopted ICF.

Figure A.2 [Bottom] shows the  $\log(\text{O}/\text{Ar})$  versus  $12 + \log(\text{Ar}/\text{H})$  distribution of these PNe coloured by their nitrogen-to-argon abundance ratio,  $\log(\text{N}/\text{Ar})$ . Young PNe, possibly affected by HBB, would show higher values of  $\log(\text{N}/\text{Ar})$  than the general trend, owing to their expected enhanced nitrogen

abundances as well as low  $\log(\text{O}/\text{Ar})$  values due to oxygen depletion. To obtain the general trend of  $\log(\text{O}/\text{Ar})$  values as a function of  $12+\log(\text{Ar}/\text{H})$ , as in Sect. 3.1, we divide the PNe into bins of  $12+\log(\text{Ar}/\text{H})$  such that there are ten PNe in each bin (the bins with the smallest and largest argon abundance have fewer measurements, five and two, respectively). We then calculate the mean and standard deviation of the  $\log(\text{O}/\text{Ar})$  values of PNe in each  $12+\log(\text{Ar}/\text{H})$  bin, shown as diamonds in Fig. A.2 [Bottom]. The PNe with the highest 25-percentile  $\log(\text{N}/\text{Ar})$  values have a mean offset of 0.02 dex ( $\sigma_{\text{offset}} = 0.11$  dex) from the general trend, while those with the lowest 75-percentile  $\log(\text{N}/\text{Ar})$  values have a mean offset of 0.01 dex ( $\sigma_{\text{offset}} = 0.14$  dex). Therefore, the PNe with higher  $\log(\text{N}/\text{Ar})$  values do not preferentially occupy lower  $\log(\text{O}/\text{Ar})$  values below the general trend. We can thus state that the number of PNe affected by HBB in our M31 sub-sample is very small and does not drive the measured  $\log(\text{O}/\text{Ar})$  trends. This is consistent with the M31 low- and high-extinction PNe having average ages  $\sim 4.5$  Gyr and  $\sim 2.5$  Gyr, respectively, with the bulk of the latter having likely formed in a burst of star formation  $\sim 2$  Gyr ago (Paper II), implying therefore a very small number of PNe with very young massive progenitors (affected by HBB).

To summarise, we find no conclusive evidence of AGB evolution effects with modification of the oxygen abundance in the nebula to be driving the trends in  $\log(\text{O}/\text{Ar})$  versus  $12 + \log(\text{Ar}/\text{H})$  for the M31 disc PNe studied in this work. Any such effect is within the measurement errors. We thus conclude the oxygen abundance measurements for M31 PNe reflect their birth ISM chemical abundances, within the errors.

## Appendix B: Chemical evolution models

Previous works to model thin and thick discs used the framework of classical, one-zone GCE models. Grisoni et al. (2017) favoured a parallel model in which thin and thick discs form simultaneously. The thin and thick disc models of the MW in Kobayashi et al. (2020a), which are plotted in Figs. 3 and 4, also follow this approach. The thick disc stars form with shorter star formation and chemical enrichment timescales than for the thin disc stars, and hence in the  $[\alpha/\text{Fe}]-[\text{Fe}/\text{H}]$  or  $\text{O}/\text{Ar}-\text{Ar}/\text{H}$  diagrams, the thick disc model appears above the thin disc model. There is a small number of old metal-poor stars in the thin disc model. On the other hand, following Chiappini et al. (1997), Spitoni et al. (2019) concluded that a two-infall model in which the thick disc form before the thin disc, with a long delay until the second infall, is better. Our models for M31 inner disc plotted in Fig. 7 also assumes two infalls.

In our two-infall models, it is assumed that two exponential infalls of primordial gas trigger two starbursts. The star formation rate is assumed to be proportional to the gas fraction (see Kobayashi et al. 2020a for the formula). Timescales of the infall ( $\tau_i$ ), star formation ( $\tau_s$ ), and outflow (if there is,  $\tau_o$ ) are determined separately. In addition three epochs are set for the truncation of the first infall (at  $t_1$ ), the onset of the second infall (at  $t_2$ ), and the truncation of the second infall (at  $t_3$ ). The initial mass function (IMF) slope is assumed to be invariant (Kroupa IMF with a slope  $x = 1.3$  at the massive end), so as for calculating the nucleosynthesis yields (Kobayashi et al. (2020a) for single stars including AGB stars and core-collapse supernovae, and Kobayashi et al. (2020b) for Type Ia supernovae) and Type Ia supernova progenitor model (Kobayashi & Nomoto 2009). Therefore, there are nine free parameters at maximum. However, it is possible to choose the best set of parameters if the following observational constraints are available: the MDF, star

**Table B.1.** Timescales of the two infall models for the M31  $2 \leq R_{\text{GC}} \leq 14$  kpc region.

	$t_1$	$t_2$	$t_3$	$\tau_{i,1} = \tau_{i,2}$	$\tau_{s,1}$	$\tau_{s,2}$	$\tau_{o,1} = \tau_{o,2}$
fiducial model	3	9	12	5	1	1	4
weaker 1st SF	2	9	-	5	5	1	3
outer disc	-	-	-	1	1	-	-

**Notes.** Summary of the timescales of the two infall models. The units are in Gyr. The timescales are: the timescales of the infall ( $\tau_i$ ), that of star formation ( $\tau_s$ ), and outflow (if there is,  $\tau_o$ ). The table lists three epochs that identify the truncation of the first infall (at  $t_1$ ), the onset of the second infall (at  $t_2$ ), and the truncation of the second infall (at  $t_3$ ), also. See Appendix B for more details.

formation rates (i.e. ages of stars), and elemental abundance ratios.

We take the observational results from Williams et al. (2017), whose sample covers the M31 inner disc and we combine them to our  $\text{O}/\text{Ar}-\text{Ar}/\text{H}$  relation at  $2 \leq R_{\text{GC}} \leq 14$  kpc. Calculating about 100 GCE models, we found this fiducial model (the solid line in Fig. B.1), which shows two similar starbursts with the same height (panel a). We note that the observational results highly depends on the input stellar evolution models (open circles for Padova, triangles for BaSTI, squares for PARSEC, and crosses for MIST).

The first starburst increases the metallicity quickly, which exceeds the super-solar metallicity at  $t \sim 3$  Gyr. Then the metallicity suddenly decrease by the second infall at  $t = 9$  Gyr, of which chemical composition is assumed to be primordial. Needless to say, with a metal-enhanced infall, the metallicity drop becomes smaller. During the break of infall ( $t = 3$  to 9 Gyr), star formation is much suppressed, but the iron abundance keeps increasing (Fig. B.1, panel b) due to the delayed enrichment from Type Ia supernovae, which is one of the two important factors to avoid the overproduction of metal-poor stars in the MDF (the G-dwarf problem, panel c). The other factor is a long infall timescale. Moderate outflow is also included, proportional to the star formation rate, in order to prevent the metallicity from becoming too high. The adopted parameters are summarised in Table B.1. As discussed, since Ar is also produced by Type Ia supernovae (Kobayashi et al. 2020b), the  $[\text{Ar}/\text{H}]$  evolution follows well the  $[\text{Fe}/\text{H}]$  evolution (panel b).

The  $\text{O}/\text{Ar}-\text{Ar}/\text{H}$  relation is shown in Fig. B.1 panel d. The plateau value is determined from the IMF-weighted yields of core-collapse supernovae. The decreasing trend is caused by 1) the knee at  $12 + \log(\text{Ar}/\text{H}) = 5.3$  caused by the dependence of argon production on the metallicity of core collapse Type II supernovae, and 2) the delayed enrichment from Type Ia supernovae at  $12 + \log(\text{Ar}/\text{H}) = 6.0$ . A loop is created by the second infall, followed by the second starburst. With outflow, the loop becomes larger. The blue dashed line is an alternative model with a weaker first star formation. Although this model produces fewer old stars in Fig. B.1 panel a, it gives a better match in Fig. B.1 panels c and d. Namely, the lack of metal-rich low- $\text{O}/\text{Ar}$  PNe prefers a weaker first starburst.

In our thin disc sample at  $R_{\text{GC}} > 18$  kpc, the  $\text{O}/\text{Ar}$  seem to be higher than these model predictions. This can be explained if the outer thin disc formed with a shorter star formation timescale, as in the model plotted in Fig. 8. The adopted timescale is even shorter than the MW thick disc and is as short as for nearby early-type galaxies.

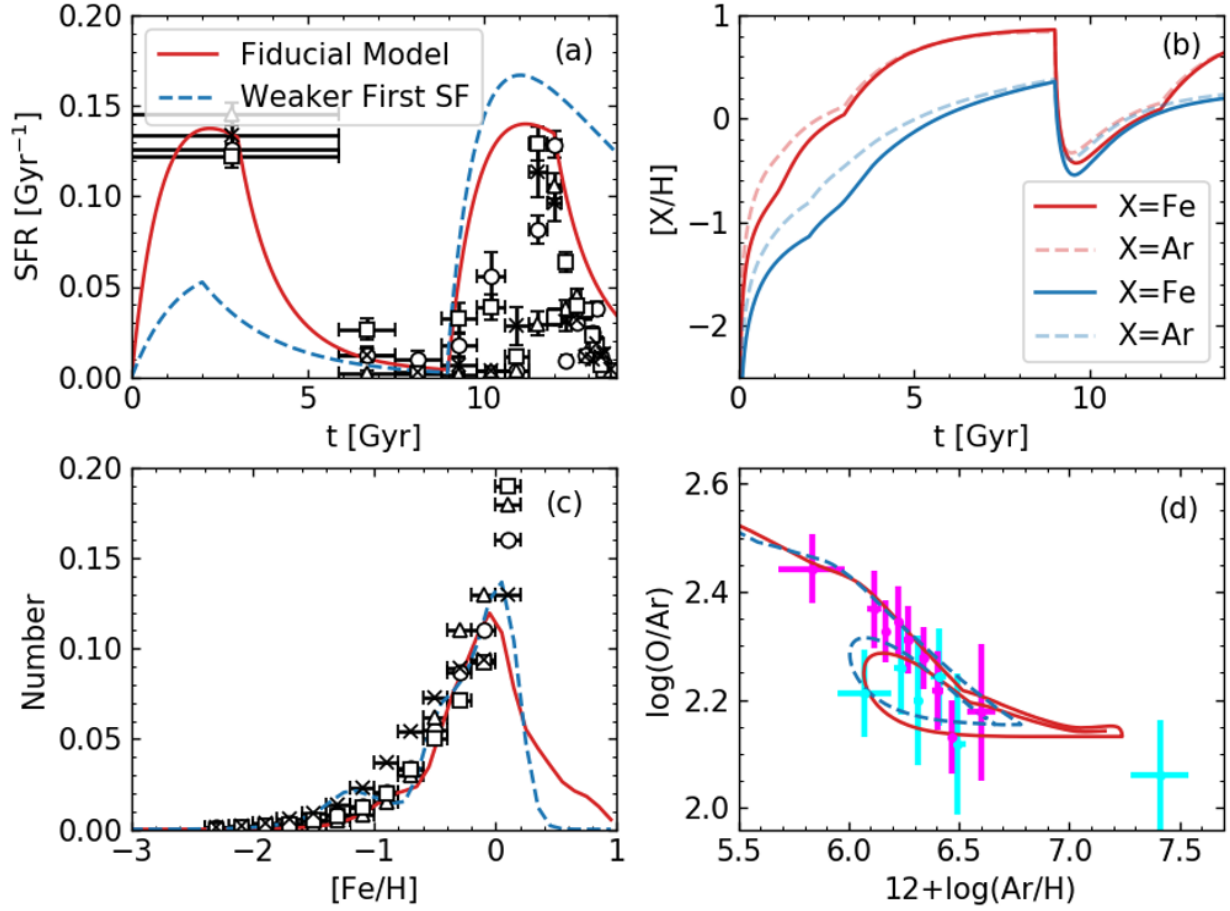


**Fig. B.1.** Chemical evolution model in the  $2 \leq R_{GC} \leq 14$  disc region. (a) Star formation history, compared to the observational results from Williams et al. (2017). (b) Evolution of iron (red and blue lines) and argon (light red and blue lines) abundances in the ISM. (c) Metallicity distribution function, compared to the observational results from Williams et al. (2017). (d) O/Ar–Ar/H relation, compared to our PN sample; magenta for low-extinction PNe over the entire M31 disc ( $R_{GC} = 2\text{--}30$  kpc) and cyan for high-extinction PNe at  $R_{GC} < 14$  kpc (same as in Fig. 7).